Draft version July 19, 2013

Preprint typeset using LaTeX style emulateapj v. 04/20/08

Subject headings: ISM: - molecular clouds – stars: formation – high mass millimeter continuum

1. INTRODUCTION

Atomic (Visbal et al 2011, Gong et al 2012, etc.) and molecular (Lidz et al 2011, etc.) transitions – such as the 21 cm spin flip transition from H°, CO (2-1), and [CII] 158μm – have been investigated as candidates for intensity mapping experiments during the Epoch of Reionization. Of these, the neutral hydrogen case is undoubtedly the most developed in terms of its standing in the literature (cf. Furlanetto, Oh, and Briggs for a review) and in the experimental arena (e.g., PAPER (Parsons et al 2010), MWA), and so interest in measuring the [CII] power spectrum, for instance, has primarily erupted as a means to complement the 21 cm studies at high redshift via the cross-correlation.

A benefit of intensity mapping over individually resolving objects is that the power spectrum is sensitive to the low luminosity galaxies that are below the detection threshold of current and future instruments. Looking forward to EoR, intensity mapping might be the only means available to observe the large population of faint galaxies responsible for reionizing the IGM, given that a telescope such as JWST will only be able to resolve down to 50 percent of UV LF at z 6 (Salvaterra et al 2011). To consider an example at lower redshifts that is *not* intensity mapping but *does* illustrate the potential of power spectra to constrain astrophysically interesting quantities, the SPIRE instrument, even, aboard Herschel misses roughly half of the sources that comprise the cosmic infrared background (CIB) at $z = X.X$ (Bethermin et al 2012). In this case, authors exploited a statistical analysis via measuring the clustering term in the angular power spectrum to uncover information about the sources that, though unresolved, nevertheless contribute to the intensity fluctuations in the SPIRE 250, 350, and 500 μm wavebands (Amblard et al 2011). From their analysis, which included a halo model approach to describing the clustering power, they were able to estimate such values relevant to galaxy evolution as characteristic mass for most efficient star formation in a host dark matter halo. With a larger survey area and an added framework to tie galaxy luminosity to the halo model, the clustering amplitude of the CIB power as measured by Herschel was used in conjunction with observed number counts above 0.1 mJy to fit various parameters (Viero et al 2012), including again the halo mass which is most efficient for hosting star formation. Despite the novelty of their approach to interpret the CIB power spectrum, Viero et al 2012 encountered significant difficulty in constraining the parameters of their model with existing data. Indeed, Penin et al (2011) explored the ability of the clustering information from CIB angular power spectra to constrain halo model parameters, and found that, while constraints are somewhat improved, simultaneously fitting for clustering data and number counts do not break the degeneracies among the halo model parameters. The authors there and in Viero et al cite unknown redshift distributions of the sources comprising the CIB as the main source of uncertainty in their analyses.

Intensity mapping, on the other hand, contains inherent redshift information encoded along the spectral dimension of the survey volume, and is thus poised to be a valuable complement to current studies of the clustering—and its evolution—of dusty star-forming galaxies at moderate redshift.

Here we examine the value of measuring power spectra of fine structure IR emission lines, including [CII]158μm, [OI]63μm, [OIII]88μm, and [SiII]35μm, at low to moderate redshifts, specifically between $z = 0.5$ and $z = 3$. As a precursor to Reionization-era experiments, the appeal as a proof-of-principle is obvious, but we focus in this paper on the ability of FIR line intensity mapped power spectra to measure the clustering amplitude of star-forming galaxies. The organization of this paper is as follows. We have calculated the mean emissivity for a suite of IR emission lines based on the IR luminosity function (Bethermin et al 2011) and empirical line to IR luminosity correlations described by Spinoglio et al (2012), and present these results in the context of a power spectrum model in Section 2. In Section 3, we envision suitable platforms—namely the SAFARI instrument aboard future space mission SPICA for the short wavelength lines and a balloon-based experiment for [CII]—for conducting the IR intensity mapping and discuss the feasibility of measuring the power spectra with error bar estimates. We also compare intensity mapping to the approach of individual line detections in order to assess its value of probing an otherwise undetected population of galaxies. Finally, in Section 4, we present preliminary results on the ability of IR line intensity mapped power spectra to discriminate between halo models.

2. SETTING UP PREDICTIONS FOR IR LINE POWER SPECTRA DURING $0.5 < Z < 3$

Traditional methods for measuring the spatial autocorrelation of galaxies through galaxy surveys rely on the knowledge of the redshift distribution of sources in the survey. Furthermore, they estimate the true three dimensional clustering of galaxies via the angular projection. Intensity mapping, however, contains intrinsic redshift information and provides a direct measure of the clustering power spectrum in three-dimensional k-space, which makes it a highly complementary probe of structure in the cosmic web.

The complete auto power spectrum of a given FIR line, X_i, as a function of wavenumber k, $P_{i,i}(k, z)$, can be separated into power from the clustering of galaxies, $P_{i,i}^{clust}(k, z)$ and a Poisson term describing their discrete nature, $P_{i,i}^{shot}(k, z)$. We compute the full nonlinear matter power spectrum, $P_{nl}(k, z)$, using the publicly available code HALOFIT+, which has been the standard tool for predicting matter power spectra upon its success in fitting state-of-the-art dark matter simulations over a decade ago (Smith et al 2003) . (We note in passing, however, that since that time, authors (cf., e.g., Takahashi et al 2012) have pointed out improvements to the halo model fit on the small scales previously inaccessible due to constraints on simulation resolution.) The clustering component of the [CII] power spectrum is then written as

$$P_{i,i}^{clust}(k,z) = \bar{I}_{[i]}^2(z)\bar{b}^2(z)P_{nl}(k,z). \quad (1)$$

Here we have implicitly assumed that the fluctuations in X_i emission trace the matter power spectrum with some average bias, $\bar{b}(z)$. The mean line intensity, $\bar{I}_i(z)$, in units of Jy sr^{-1}, can be calculated as

$$\bar{I}_i(z) = \int \mathrm{d}n_i \frac{L_i}{4\pi D_L^2} y_i D_A^2, \quad (2)$$

where the integration is taken with respect to n_i, the number of galactic X_i emitters per cosmological comoving volume element. (The factor y_i is the derivative of the comoving radial distance with respect to the observed frequency, i.e. $y = d\chi/d\nu = \lambda_{i,rest}(1+z)^2/H(z)$, and D_A is the comoving angular distance.)

Finally, the shot noise component of the total intensity mapped power spectrum—with the same units as the clustering term, namely, Jy sr^{-1}(Mpc h^{-1})^3—takes the form

$$P_{i,i}^{shot}(k) = \int \mathrm{d}n_i \left(\frac{L_i}{4\pi D_L^2}\right)^2 \left(y_i D_A^2\right)^2. \quad (3)$$

2.1. *Calculating IR line volume emissivity*

The number density and the luminosity of [CII] emitters that appear in equations (2) and (3) can be derived by a variety of methods. In earlier papers on intensity mapping of molecular and fine-structure emission lines at high redshift (z $\gtrsim$ 6), a common approach involved using the dark matter halo mass function in lieu of the [CII] emitter density (and invoking a one-to-one correlation between halos and galaxies, which is not unreasonable at high redshifts). The [CII] luminosity, in turn, could be scaled according to the star formation rate, which was related to halo mass via a proportionality constant comprised of factors that described the fraction of baryons available for star formation, as well as the dynamical timescale for star formation. While this theoretical model is feasible at high redshift to provide an estimate on the volume emissivity, we take advantage of the relative wealth of observations of [CII] luminosities in individual galaxies, IR galaxy number counts, and cosmic star formation rate density at the low redshifts (relevant to this study). To this end, we first employ the empirically-constrained, backwards-evolution model of the IR luminosity function $\Phi(L_{IR}, z)$ from Bethermin et al (2011, hereafter B11) to predict the number of galaxies with luminosity L_{IR} at a given redshift in some comoving volume of the Universe per logarithmic luminosity interval, i.e., $\frac{\mathrm{d}N(L_{IR},z)}{\mathrm{d}V\mathrm{dlog}_{10}L_{IR}}$ or $\frac{\mathrm{d}n_{IR}}{\mathrm{dlog}_{10}L_{IR}}$. To convert the infrared luminosity to a line luminosity in [CII], we apply the relation for $L_{[\mathrm{CII}]}$ as a function of L_{IR} provided by Spinoglio et al (2012). The fit in their paper was based on the collection of ISO-LWS observations of local galaxies in Brauher et al (2008), and is reproduced below:

$$L_{[\mathrm{CII}]}(L_{\mathrm{IR}}) = (0.89\pm0.03)\log_{10}L_{\mathrm{IR}} - (2.44\pm0.07)L_{\mathrm{IR}}. \quad (4)$$

Thus, it becomes possible to write the cosmic mean intensity and shot noise of [CII], in units of Jy sr^{-1}, as a function of redshift based on the B11 luminosity function and Spinoglio et al (2012) $L_{[\mathrm{CII}]} - L_{\mathrm{IR}}$ relation as

$$\bar{I}_{[\mathrm{CII}]}(z) = \int \mathrm{d}L_{IR}\Phi(L_{IR},z)\frac{f_{[\mathrm{CII}]}}{4\pi D_L^2}\frac{1}{\ln 10} y D_A^2 \quad (5)$$

$$P_{shot}(z) = \int \mathrm{d}L_{IR}\Phi(L_{IR},z)\frac{f_{[\mathrm{CII}]}}{4\pi D_L^2}\frac{L_{IR}f_{[\mathrm{CII}]}}{4\pi D_L^2}\frac{1}{\ln 10}\left(yD_A^2\right)^2 \quad (6)$$

where $f_{[\mathrm{CII}]}$ is the fraction of IR luminosity emitted in [CII], as computed from equation (4).

It should be noted that the mean [CII] luminosity $\bar{L}_{[CII]}$ does, in reality, include a contribution from diffuse gas in the intergalactic medium (IGM), yet Gong et al (2012) estimated that the specific intensity coming from the IGM ranges from $\sim 10^{-3}$ Jy sr^{-1} to ~ 1 Jy sr^{-1} for different physical conditions in the ISM at $z = 1$—a negligible amount compared to the emission from the interstellar medium (ISM) of galaxies.

The resulting mean intensities for a suite of FIR lines is plotted in Figure 1 as functions of redshift and observed frequency. $\bar{I}_\nu$ vs λ_{obs} can be interpreted as identifying the dominant source of fluctuations, according to our model, for a given frequency. Such an identification becomes useful in the practical discussion of identifying sources of signal contamination to the target line in question (section X.X).

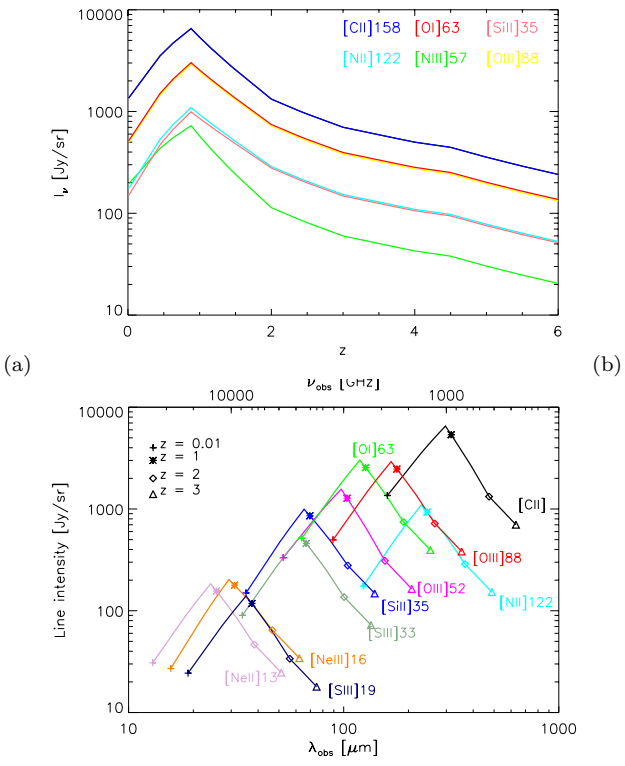

FIG. 1.— Intensity of fine structure line emission plotted versus redshift (*top*) and observed wavelength (*bottom*) as predicted from Spinoglio line luminosity fits as applied to the Bethermin (2011) luminosity function.

3. ATP: WHEN TO INTENSITY MAP?

The principal advantage of intensity mapping over individual detections is encapsulated in Figure XXX, which shows predictions of the [SiII]35μm power spectrum at $z = 3$ with a mere 45 hours of observing time over a survey area of 0.5 deg^2. The power spectrum in this figure is constructed in two ways: (1) with the lower limit of the IR luminosity function fixed at 10^8 L$_\odot$ (*solid blue curve*) and (2) with the lower limit replaced by the 5σ-0.1hr detection threshold corresponding to SPICA-SAFARI (*solid magenta curve*). Note that the luminosity function enters into the power spectrum (equation 4) through equations (2) and (5). With 45 hours of observing at $z = 3$, the detection limit for SAFARI is 1.3×10^{13} L$_\odot$, *whichmeansthat, accordingtotheBetherminluminosityfunction, virtuallyall[SiII]sourceshavelineluminositiesbelowthethr* $\times 10^{12}$ L$_\odot$ and the percentage of galactic emitters below this threshold is 80%. (In fact, Spinoglio et al find only a couple of galaxies with normal-type luminosities in their 0.5 deg^2 field after 450 hours of integration.) While this missing fraction of the [SiII]-emitting population dramatically diminishes the signal in the power spectrum computed by integrating the luminosity function upwards from the SAFARI sensitivity, the power spectrum computed via intensity mapping, which probes the full range of luminosities in the luminosity function, has relatively high SNR of 40. In this case, intensity mapping becomes an efficient use of telescope observation time, and a unique probe of the low luminosity population.

Furthermore, shallow and large area surveys of the FIR emission lines provide a means of connecting large scale structure with galaxy evolution, and intensity mapping can be complementary to individual detections when the area mapped by an observing platform becomes large enough that the required observing time for such a measurement is prohibitive. For example, we consider again the SAFARI instrument aboard SPICA. To map an area of 8.1 deg^2, which probes scales down to $k = 0.07$ h/Mpc, with SPICA's 2 arcmin by 2 arcmin field of view would necessitate 7,400 hours of observing time to achieve one hour of integration time per field. If one were to observe the same volume with intensity mapping, on the other hand, it would only be necessary to observe for a relatively modest 450 hours in order to recover high SNR on the power spectrum of a bright line such as [OI]63 (Figure XXX). For comparison, 450 hours of observing via traditional individual detections would amount to 0.06 hr of observing time per field, which means that only galaxies with IR luminosities above 2.3×10^{12} L$_\odot$ would be observed in [OI]63.

4. OBSERVATIONAL STRATEGY

Include plot of fraction of emissivity vs $L_{IR,min}$ to further motivate intensity mapping observation of clustering.

4.1. *[CII] power spectrum*

Atmospheric transmission permits uninterrupted spectral coverage for a balloon experiment in the wavelength range 240 to 420 μm, or $z = 0.5 - 1.5$ for [CII]158. For concreteness in our discussion of the detectability of the [CII] power spectrum, we sketch the envisioned balloon-borne experiment with various aperture diameters, $D_{ap} = 1.0$ and 3.0 m, and survey areas, $A_{survey} =$

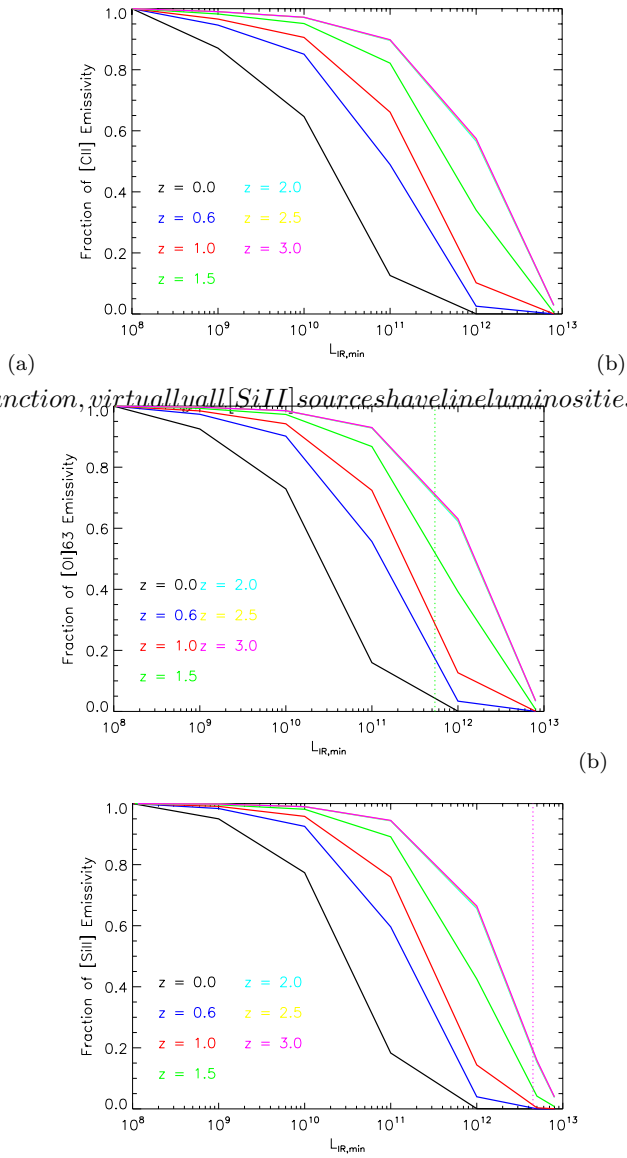

FIG. 2.— Fraction of emissivity recovered by integrating the luminosity function using various minimum L_{IR} values. The upper limit for integration is fixed at 10^{13} L$_\odot$.

0.1, 1.0, and 10.0 deg^2. Relevant parameters for the experimental platforms envisioned here are summarized in Table 1.

Predictions—as computed from the method of combining the cosmological matter power spectrum and the IR LF model outlined in Section 2.1—for the [CII] power spectrum at four redshifts $z = 0.63, 0.88, 1.16$, and 1.48 in the above redshift range are displayed in Figure 4 for the fiducial case a 3 meter aperture, 1.0 deg^2 survey area, and total observing time, $t_{obs}^{survey} = 200$ hours. (Note that we use $\Delta^2_{[CII]} = k^3 P_{[CII],[CII]}(k)/(2\pi^2)$ when plotting the power spectrum, where the integral of $\Delta^2_{[CII]}$ over logarithmic k bins is equal to the variance in real space.) At these redshifts, respectively, the average linear bias has been assumed to be $\bar{b} = 2.0, 2.3, 2.6$, and 2.9, in line with theoretical predictions. We calculate error bar estimates and the mean signal to noise ratio (SNR)

for each power spectrum by assuming a spectrally flat noise power spectrum, so that the noise power in each pixel, P_N, is calculated from

$$P_N = \sigma_N^2 \frac{V_{pix}}{t_{obs}^{pix}}, \tag{7}$$

where σ_N^2 is the instrument sensitivity (NEI, in units of Jy sr^{-1} Hz$^{-1/2}$, V_{pix} is the volume of a pixel, and t_{obs}^{pix} is the time spent observing on a single pixel. The variance of a measured k, $\sigma^2(k)$, is then written as

$$\sigma^2(k) = \frac{\left(P_{[CII],[CII]}(k) + P_N(k)\right)^2}{N_{mode}}, \tag{8}$$

where N_{mode} is the number of wavemodes that are sampled for a given k bin of some finite width $\Delta\log(k)$. (We have chosen $\Delta\log(k) = 0.3$ for this analysis.)

The k-averaged SNR, in turn, is calculated from the expression

$$SNR = \sqrt{\sum_{bins} \left(\frac{P_{[CII],[CII]}(k)}{\sigma(k)}\right)^2} \tag{9}$$

Note that It is possible to rewrite P_N in terms of the parameters from Table 1, giving

$$\begin{aligned} P_N &= \sigma_N^2 A_{pix} \Delta r_{los}^{pix} / \frac{t_{obs}^{survey}}{n_{beams}/N_{instr}^{spatial}} \\ &= \sigma_N^2 A_{pix} \Delta r_{los}^{pix} / \frac{t_{obs}^{survey} N_{instr}^{spatial}}{A_{survey}/A_{pix}} \\ &= \sigma_N^2 \frac{\Delta r_{los}^{pix} A_{survey}}{t_{obs}^{survey} N_{instr}^{spatial}} \end{aligned} \tag{10}$$

In this form, it becomes apparent that—with fixed number of spatial pixels, spectral resolution, and total observing time—the only factor driving up the amplitude of noise power is the survey area; the effect of increasing aperture only allows access to higher wavenumbers. This behavior is shown clearly in Figure 5, where the SNR is plotted as a function of k for different survey geometries and both mirror diameters. Also seen in Figure 5, the greater number of wavemodes sampled (entering as $N_{modes}^{-1/2}$ in the expression for σ) with the larger survey area does not necessarily compensate for the the increase in P_N. For example, the factor of ten increase in P_N going from $A_{survey} = 1$ to 10 deg^2 is only overcome by the additional modes in the larger survey area for $k < 1$, leading to a higher S/N for these modes. At $k > 1$, the S/N in each mode for the 1 and 10 deg^2 fields becomes comparable.

4.2. *[OI]63, [SiII]35, and other IR line power spectra*

5. INTENSITY MAPPED LINE RATIOS AND THE CROSS POWER SPECTRUM

Visbal and Loeb (2010) showed how the cross spectra can be used to differentiate between a target line and a contaminating line (or "bad line", in their words). The cross power spectrum of two distinct lines can generally be written

$$P_{i,j}(k) = \bar{S}_i \bar{S}_j \bar{b}_i \bar{b}_j P_{lin}(k) + P_{shot}^{i,j}(k) \tag{11}$$

- Discuss Spinoglio and Cloudy predictions for [CII]/[NII] as a function of galaxy IR luminosity

[h]

	ICarIS	SPICA-SAFARI
Target Line	[CII]158μm	[OI]63μm
Redshift	1.5	1.5
Aperture (m)	3.0	3.0
A_{survey} (deg^2)	1	1
R	450	2000
λ_{center} (μm)	393	160
θ_{FWHM} (")	33	13
Line Sensitivity (W m^{-2} sec$^{1/2}$)	7.1 $\times 10^{-18}$	2.0 $\times 10^{-19}$
NEI (Jy sr^{-1} sec$^{1/2}$)	1.0 $\times$ 10^7	1.3 $\times$ 10^7
V_{voxel} (Mpc^3 h^{-3})	5.8	0.53
Bandwidth (GHz)	108	350*
$\Delta\nu$ (GHz)	1.7	0.94
t_{obs}^{survey} (hr)	200	1000
t_{obs}^{voxel} (hr)	0.4	1.1
N_{beam} (deg^{-2})	11,926	71,951
signal (Jy sr^{-1})	2,593	1,373
P_{noise} (Jy^2 sr^{-2} Mpc^{-3} h^3)	4.0 $\times 10^{11}$	9.6 $\times 10^{10}$
N_{modes}^{obs}	3.7 $\times$ 10^5	1.3 $\times$ 10^7
SNR(k = 0.16 h Mpc^{-1})	5.4	3.1
SNR(k = 2.6 h Mpc^{-1})	24	130

TABLE 1
Experimental Parameters for Envisioned Balloon Experiment at $z = 0.88$

t_{obs}^{survey} (hr)	200					
$I_{[CII]}$ (Jy sr^{-1})	6.27×10^3					
NEI (Jy sr^{-1} sec$^{1/2}$)	2.17×10^7					
B_ν (GHz)	945-1,086					
δ_ν (GHz)	2.25					
A_{survey} (deg^2)	0.1		1.0		10.0	
V_{survey} (Mpc$^3 h^{-3}$)	2.87×10^4		2.87×10^6		2.87×10^8	
D_{ap} (m)	1	3	1	3	1	3
Beam FWHM (arcmin)	0.42	1.25	0.42	1.25	0.42	1.25
V_{voxel} (Mpc$^3 h^{-3}$)	19.76	2.20	19.76	2.20	19.76	2.20
t_{obs}^{voxel} (hr)	2.0×10^2	2.3×10^1	2.1	2.3×10^{-1}	2.1×10^{-2}	2.3×10^{-3}
P_N^{voxel} (10^{10} Jy^2 sr^{-2} Mpc^3 h^{-3})	1.17	1.17	117	117	11, 700	11, 700

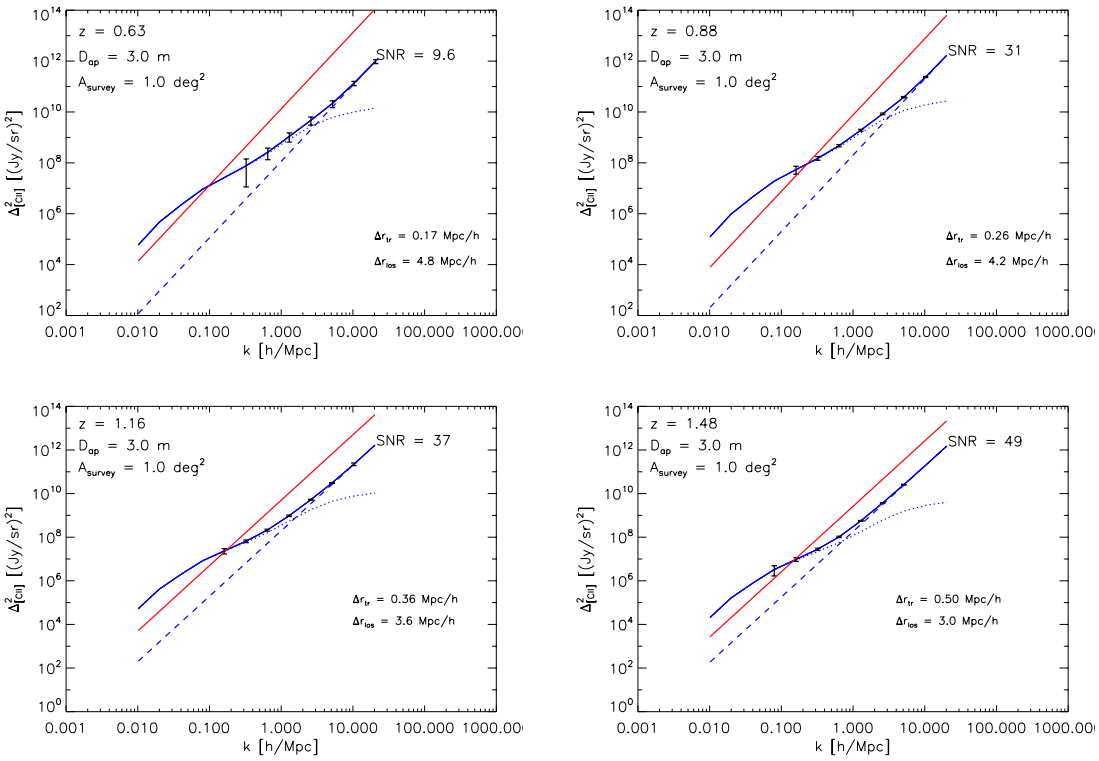

Fig. 3.— Predicted [CII] power spectra with error estimates from $z = 0.63$ to $z = 1.48$ for telescope with 3 meter aperture and a survey area of 1 square degree. Blue, green, magenta, and cyan curves denotes power spectra computed with upper limits of $L_{IR} = 10^{13}, 10^{12}, 10^{11}$, and 10^{10} L$_\odot$, respectively.

TABLE 2
Experimental Parameters for SPICA-SAFARI Survey of [OI]63 at $z = 1.5$

k_{fund} (h Mpc^{-1})	0.03		0.05		0.07	
NEI (10^6 Jy sr^{-1} sec$^{1/2}$)	6.2		6.2		6.2	
A_{survey} (deg^2)	44		16		8.1	
r_{perp} (Mpc h^{-1})	360		220		160	
B_ν (GHz)	360		220		160	
$\Delta\nu$ (GHz)	4.25		4.25		4.25	
n_{beams} (10^6 beams)	3.3		1.1		0.61	
t_{obs}^{survey} (hr)	450	1,000	450	1,000	450	1,000
t_{obs}^{pix} (sec)	40	88	110	240	220	480
P_N (10^{10} Jy^2 sr^{-2} Mpc^3 h^{-3})	12	5.3	4.2	1.9	2.2	0.97

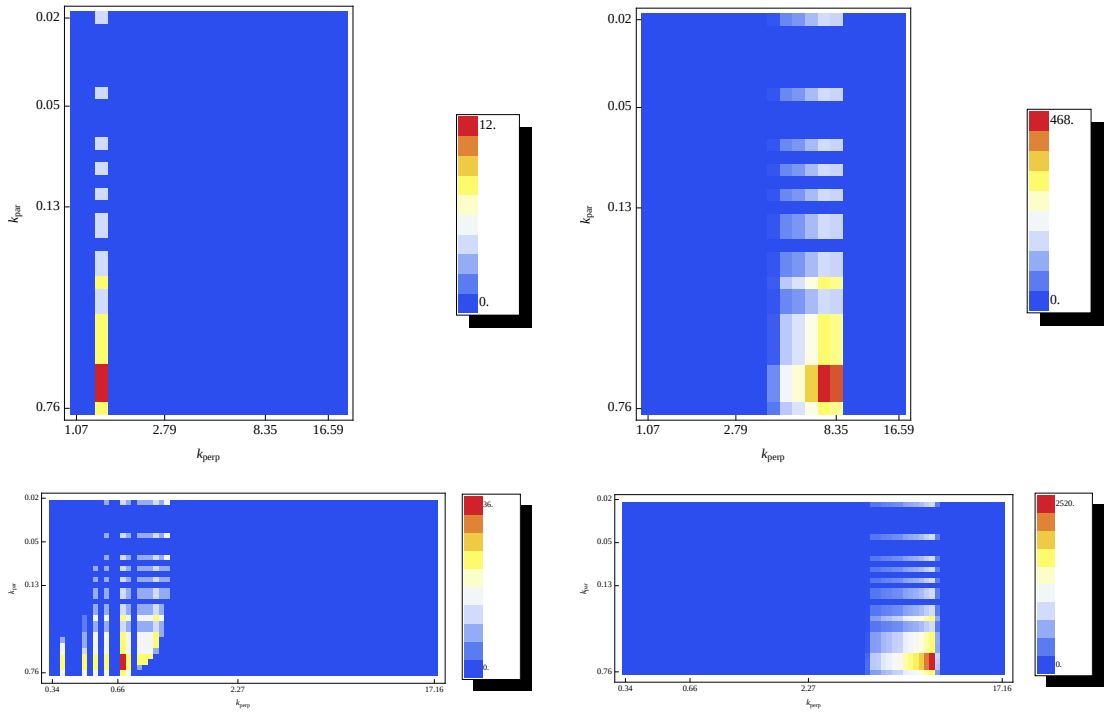

FIG. 4.— Sample histogram of k_{par}-k_{perp} for ICarIS [CII] power spectrum at $z = 0.88$, $D_{ap} = 3.0$m and $A_{survey} = 1.0$ deg^2.

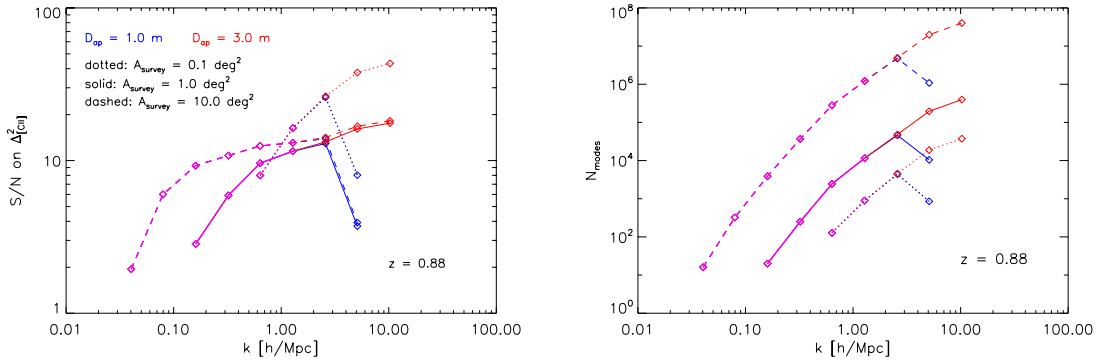

FIG. 5.— Signal to noise on the dimensionless [CII] power spectrum $\Delta^2_{[CII]}$ and number of modes as a function of k. The blue lines represent S/N for the 1 meter aperture, red denotes a 3 meter aperture, and purple shows where the two overlap. Survey areas of 0.1, 1, 10 square degree fields are shown as the solid, dashed, and dotted lines, respectively. The special case of a line scan survey with dimensions 1 degree by 1 beam for a 3 meter aperture is plotted as the dash-dotted line.

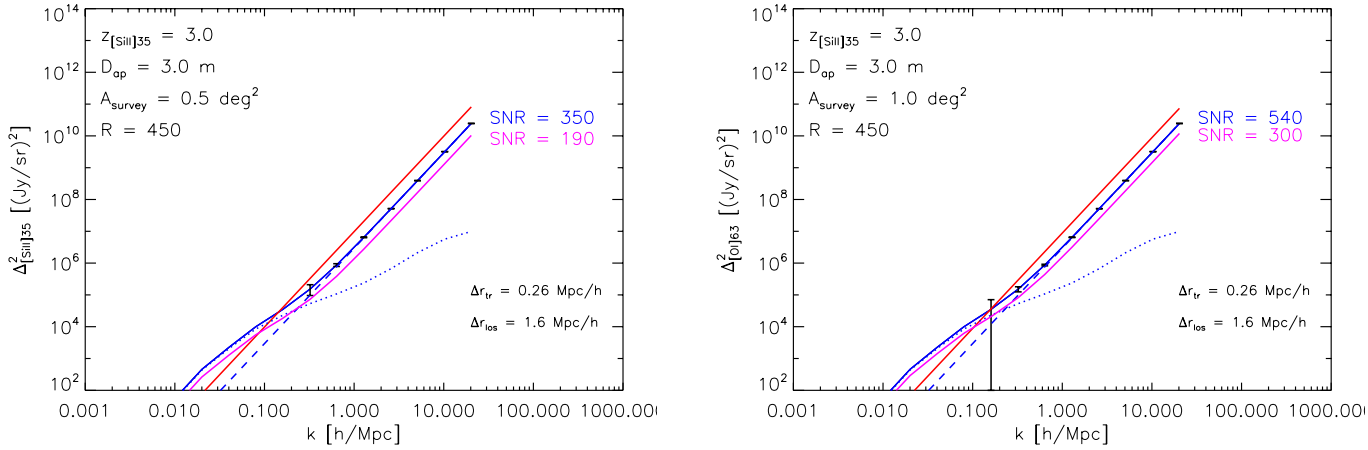

FIG. 6.— Predicted [SiII]35 power spectra at $z = 3$ for SPICA-SAFARI and survey area $A_{survey} = 0.5$ deg^2 and 1.0 deg^2 with $t_{obs}^{survey} = 450$ hr and 1,000 hr, resp. The power spectrum computed by integrating the IR LF over the full range of luminosities (blue curve) is being compared to the power spectrum computed by integrating the IR LF up to the sensitivity in L_{IR} for SAFARI (magenta curve).

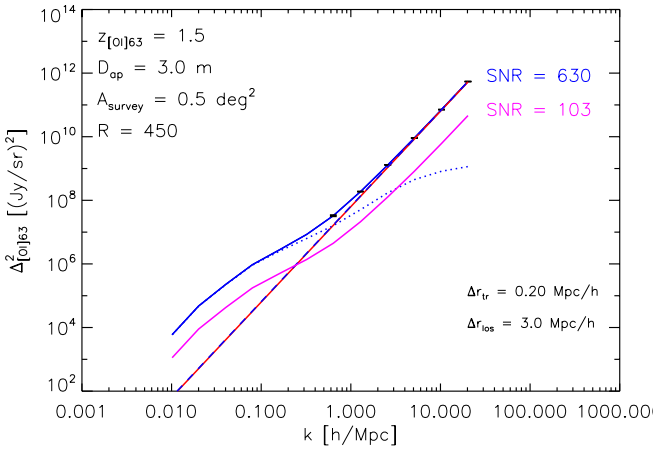

FIG. 7.— Predicted [OI]63 power spectra at $z = 1.5$ for SPICA-SAFARI and survey area $A_{survey} = 0.5$ deg^2 with $t_{obs}^{survey} = 450$ hr. The power spectrum computed by integrating the IR LF over the full range of luminosities (blue curve) is being compared to the power spectrum computed by integrating the IR LF up to the sensitivity in L_{IR} for SAFARI (magenta curve).

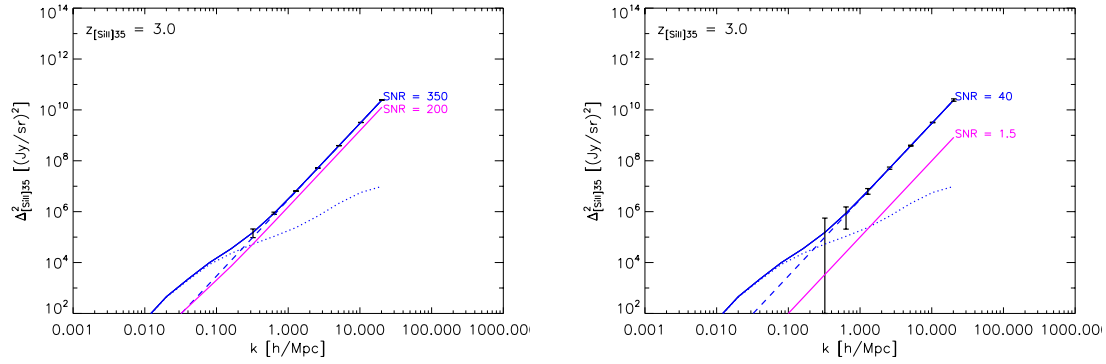

FIG. 8.— [SiII]35μm power spectra at $z = 3$ with observing time of 450 and 45 hours.

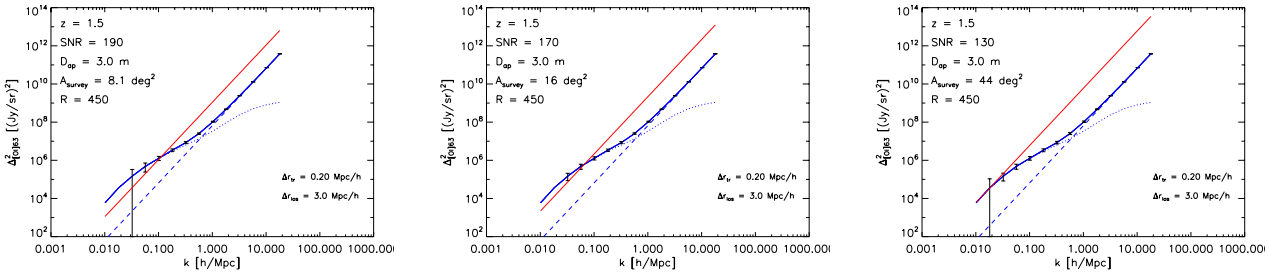

FIG. 9.— [OI]63μm power spectra at $z = 1.5$ with observing time of 450 hours. Fundamental k modes = 0.7, 0.5, 0.3 h/Mpc.

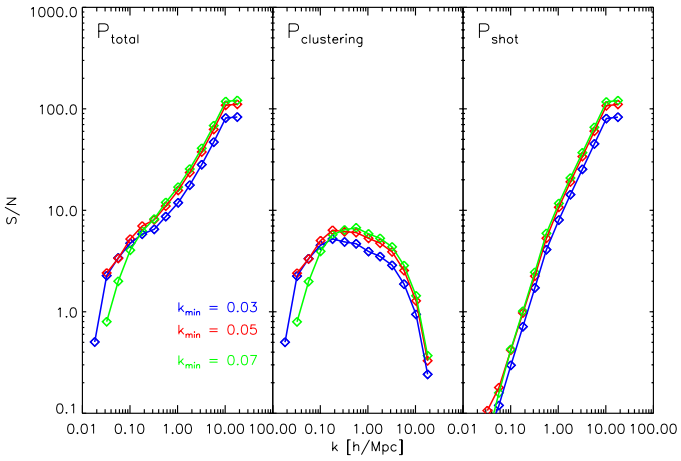

FIG. 10.— SNR vs k for predicted SAFARI power spectrum of [OI]63μm at z = 1.5, with 450 hours of observing time.

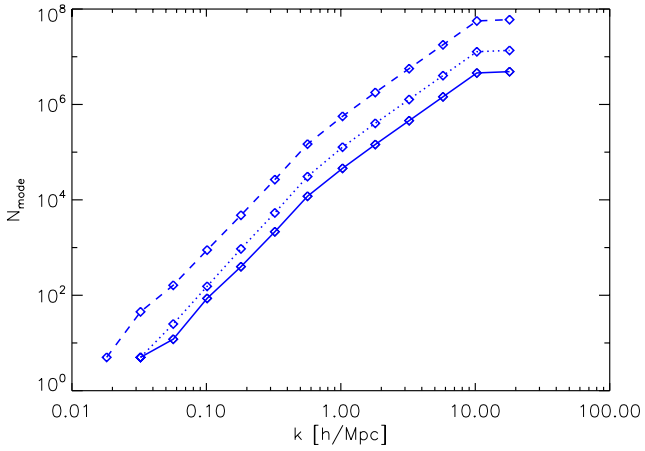

FIG. 11.—

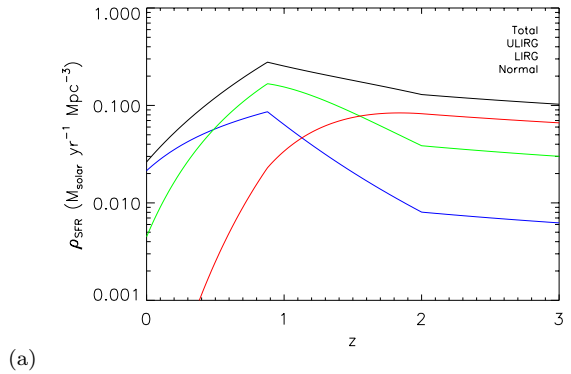

(a)

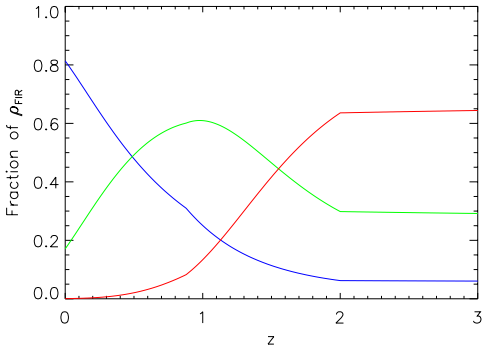

(b)

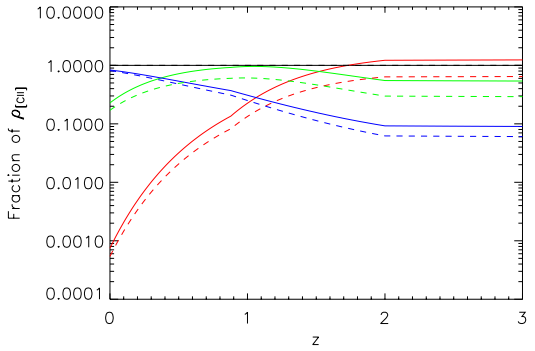

(c)

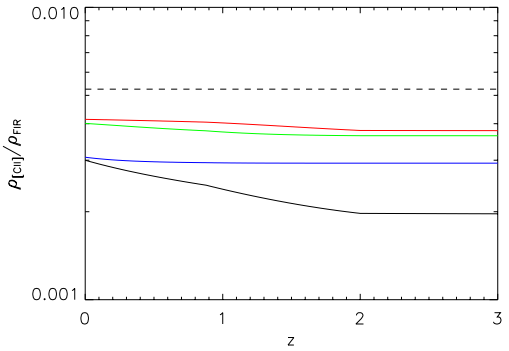

(d)

FIG. 12.— Redshift evolution of the star formation rate (a), FIR luminosity (b), [CII] luminosity (c), and $[CII]-L_{FIR}$ relation (d) based on the Bethermin et al (2011) IR luminosity function. In panels (a)-(c), the red, green, and blue colors denote contributions to the luminosity function by ULIRGs, LIRGs, and normal galaxies, respectively, and black lines denote a total. The bottom two panels incorporate two prescriptions for finding $L_{[CII]}$: (1) $L_{[CII]}$ as a function of L_{IR} from Spinoglio et al (2012) (*solid lines*) and (2) $L_{CII} = 0.003 \times L_{FIR}$ (*dashed lines*). In panel (d), the red, green, and blue line represent the mean $[CII]-L_{FIR}$ for their respective classes. Note there is no externally imposed redshift evolution on the [CII] luminosity in all cases.

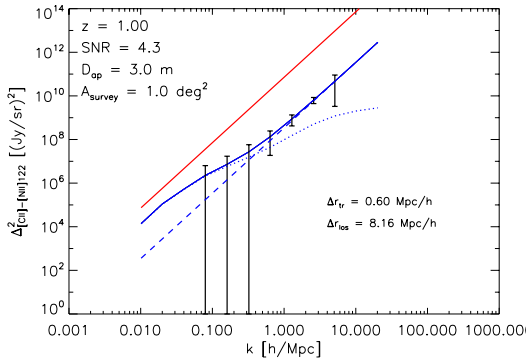

FIG. 13.— Predicted cross power spectrum $P_{[CII]-[NII]}$ at $z = 1$ for D_{ap}= 3.0 and A_{survey} = 1.0 deg^2.